Hindawi
International Journal of Antennas and Propagation
Volume 2023, Article ID 8872629, 12 pages
https://doi.org/10.1155/2023/8872629

Research Article

Liquid Crystal Polymer-Based Flexible Trap Ultra-Wideband Antenna Design

Xinwei Wang,[1] **Zhaoyang Xue**,[1] **Qing Liang**,[1] **Wei Xiong**,[2] **and Zhiyao Zhang**[1]

[1]*Xi'an University of Posts and Telecommunications, School of Electronic Engineering, Xi'an, Shaanxi, China*
[2]*Xi'an FanYi University, School of Information Engineering, Xi'an, Shaanxi, China*

Correspondence should be addressed to Zhaoyang Xue; xuezhaoyang@stu.xupt.edu.cn

Received 6 June 2023; Revised 21 November 2023; Accepted 11 December 2023; Published 26 December 2023

Academic Editor: Rajkishor Kumar

Copyright © 2023 Xinwei Wang et al. This is an open access article distributed under the Creative Commons Attribution License, which permits unrestricted use, distribution, and reproduction in any medium, provided the original work is properly cited.

The wearable ultra-wideband antenna that is appropriate for body area networks is designed and implemented in this article. Stepped circular radiation patches, microstrip feeders, and trapezoidal floors make up the majority of the antenna. Good bending qualities have been attained by using liquid crystal polymer, a flexible material, as a dielectric substrate. An antenna measuring 30 mm × 35 mm × 0.1 mm was designed with two C-shaped slots etched on it to achieve notch function in the 3.20–4.10 GHz and 5.19–5.98 GHz frequency bands. Its working frequency range was 1.96–11.61 GHz, and its specific absorption rate for the human body was less than 2 W/kg. The test findings demonstrate that ultra-wideband body area network systems can be implemented using the antenna impedance and radiation characteristics.

1. Introduction

Since 2002, when the Federal Communications Commission (FCC) allocated the 3.1–10.6 GHz band to the civil ultra-wideband (UWB) technology, it has received a lot of attention in the field of wireless communication because of its advantages of low power consumption, high accuracy, and low complexity [1, 2]. The performance of antennas will have the most direct impact on the overall performance of wireless communication. Ultra-wideband antennas have the advantages of high transmission efficiency, high processing gain, good concealment, high multipath resolution, low cost, and low power consumption [3]. It is with these advantages that ultra-wideband technology is widely used in high-precision positioning, high-speed multimedia wireless communication, radar, control, medicine, and other fields [4].

The research direction of ultra-wideband antennas is mainly focused on the traditional bandwidth as well as on the antenna [5, 6] size, where microstrip antennas have significant advantages over other forms of antennas [7]. In the literature [8], a tapered slot UWB antenna was designed to increase the bandwidth and reduce the area of the antenna by etching a series of rectangular slot lines, and the bandwidth was increased by 4.72 GHz compared to that without the etched slot lines. The UWB antenna designed in the literature [9] was fed by microstrip lines and operated from 2.8 to 12.5 GHz, and the bandwidth was extended by increasing the resonant point by etching the slot lines on the ground plate.

In addition to this, another key issue of ultra-wideband antennas is the interference of narrowband signals in the ultra-wideband band [10]. To solve the interference of narrowband signals, the trapping function is designed. Currently, the main methods to achieve trapping are etching geometric slits of different shapes [11], placing parasitic cells, and adding resonant branches [12]. In the literature [13], an ultra-wideband antenna with trapping characteristics was proposed to achieve the trapping function in the 5.3–5.8 GHz and 7.85–8.55 GHz bands by adding two different sizes of open resonant ring SRRs next to the microstrip feed line. However, when the antenna operates at a low-frequency band, the placed parasitic units and the added resonant branches are too long, which increases the antenna size and is not conducive to antenna miniaturization. In the paper [14], a "swan-" shaped ultra-wideband

antenna is designed to avoid interference from WLAN systems by etching a "U-" shaped gap in the microstrip feed line. The ultra-wideband antenna proposed by the authors in reference [15] has an operating bandwidth of 2.5–12 GHz, and the trap function in the operating band is achieved by etching slot lines on the radiating patch and loading the electromagnetic band gap structure (EBG) on the side of the microstrip feed line. A circular nested UWB antenna was designed in the literature [16]. The introduction of the electromagnetic band gap structure (EBG) at the center of the front of the dielectric substrate makes the antenna produce the trap feature at 4.0–5.2 GHz, and the antenna size is 60 mm × 60 mm, which is large and can suppress the interference in only one frequency band. The dielectric substrate of these ultra-wideband antennas [17] is generally made of rigid material, which is less flexible and cannot meet the application of the wearable system and body area network WBAN.

With the development of miniaturization and convenience of electronic communication devices and wearable terminal devices, many antennas using flexible materials as dielectric substrates have emerged. In the literature [18], a flexible ultra-wideband antenna is proposed, which is fabricated by miniaturized full inkjet printing and has an operating bandwidth of 3.43–10.1 GHz and no trap function. In reference [19], a wearable antenna is designed for wireless body area networks with an operating bandwidth of 4.55–13 GHz, using a flexible textile substrate with a thickness of 4.68 mm and no trap band. In the literature [20], an ultra-wideband antenna for a body area network is designed with a three-petal flower-shaped patch printed on a substrate of jeans fabric with an antenna size of 60 mm × 60 mm × 2.16 mm and with no trapping functions.

In this paper, a flexible band trap ultra-wideband antenna based on LCP (liquid crystal polymer) is designed. A novel polymer material called liquid crystal polymer (LCP) has good bending properties, which can be used to create antennas that are appropriate for wearable technology and body area networks. In this work, we designed an ultra-wideband antenna with a liquid crystal polymer dielectric substrate. The antenna size is 30 mm × 35 mm × 0.1 mm, and its operating band range is 1.96–11.61 GHz. It is fed by a coplanar waveguide, which makes it easy to integrate into the circuit. The antenna is made up of a modified radiation patch, a 50 Ω microstrip feed line, and a trapezoidal ground plate. Etching slits on the radiation patch can suppress 3.20–4.4 GHz. It is able to suppress the interference in the bands of 3.20–4.10 GHz and 5.19–5.98 GHz. The effect of flexible bending of the antenna on the S-parameters is also analyzed, and the effect on the human-specific absorption rate is experimented.

2. Antenna Design and Analysis

2.1. Antenna Structure Design. Figure 1(a) illustrates the antenna structure which was designed in this paper. The processed antenna is physically depicted in Figure 1(b). The size of the antenna is ($L \times W$) 35 mm × 30 mm. Liquid crystal polymer is used as the dielectric substrate, the relative dielectric constant is 2.9, the loss angle tangent is 0.002, and the thickness of the dielectric substrate is 0.1 mm.

A modified rectangular plus semicircular patch, a 50 Ω microstrip feed line, and a trapezoidal grounding plate make up the antenna unit. By cutting the corners of the floor and rounding the corners of the patch, the antenna's bandwidth can be expanded. The antenna is fed by a coplanar waveguide. The dual trap characteristics of the WLAN band and WiMAX band are obtained by etching two C-shaped slits in the radiating patch to prevent interference from narrowband signals. The length of the etched C-shaped slit is determined by the following equation, where f_{notch} is the trap center frequency, ε_e is the effective permittivity, ε_r is the relative permittivity, c is the speed of light in free space, and L is the slit length.

$$L = \frac{c}{2 f_{\text{notch}} \sqrt{\varepsilon_e}},$$
$$\varepsilon_e = \frac{\varepsilon_r + 1}{2}, \tag{1}$$
$$L_{\text{notch}} = \frac{c}{f_{\text{notch}} \sqrt{2(\varepsilon_r + 1)}}.$$

Table 1 gives the optimized antenna parameters, according to the data processed and produced by the antenna physically as shown in Figure 1.

2.2. Antenna Design Process. The antenna's design process is shown in Figure 2. Two rectangular grounding surfaces, called Ant-a, and a rectangle radiating patch make up the antenna in Figure 2(a). Then, in Figure 2(b), the top of the rectangular radiation patch is improved to be semicircular, and the rounded corners are cut on both sides of the patch, named Ant-b. In Figure 2(c), the bottom of the radiation patch is improved by cutting the rounded corners, named Ant-c. In Figure 2(d), the rectangular ground plane is improved to a trapezoidal ground plane, named Ant-d. The comparison of the four antennas' return loss simulation results is displayed in Figure 3.

The design process of the antenna is shown in Figure 2, and the results of the S-parameters in the design process are shown in Figure 3. From the loss curve in the figure, it can be seen that the antenna in step 1 is obtained by estimating the patch size through the equivalent cylindrical method, and the antenna bandwidth is 2.13–4.55 GHz at this time, which is insufficient for ultra-wideband communication. Steps 2 and 3 improve the resonant frequency and further expand the bandwidth of the antenna by improving the top of the patch with a semicircular shape and cutting the bottom with rounded corners. Finally, step 4 improves the resonant frequency and S_{11} parameters of the antenna by changing the rectangular floor to a trapezoidal floor, and after the abovementioned steps, the bandwidth of the antenna is 2.17–11.74 GHz with the basic performance of the ultra-wideband antenna.

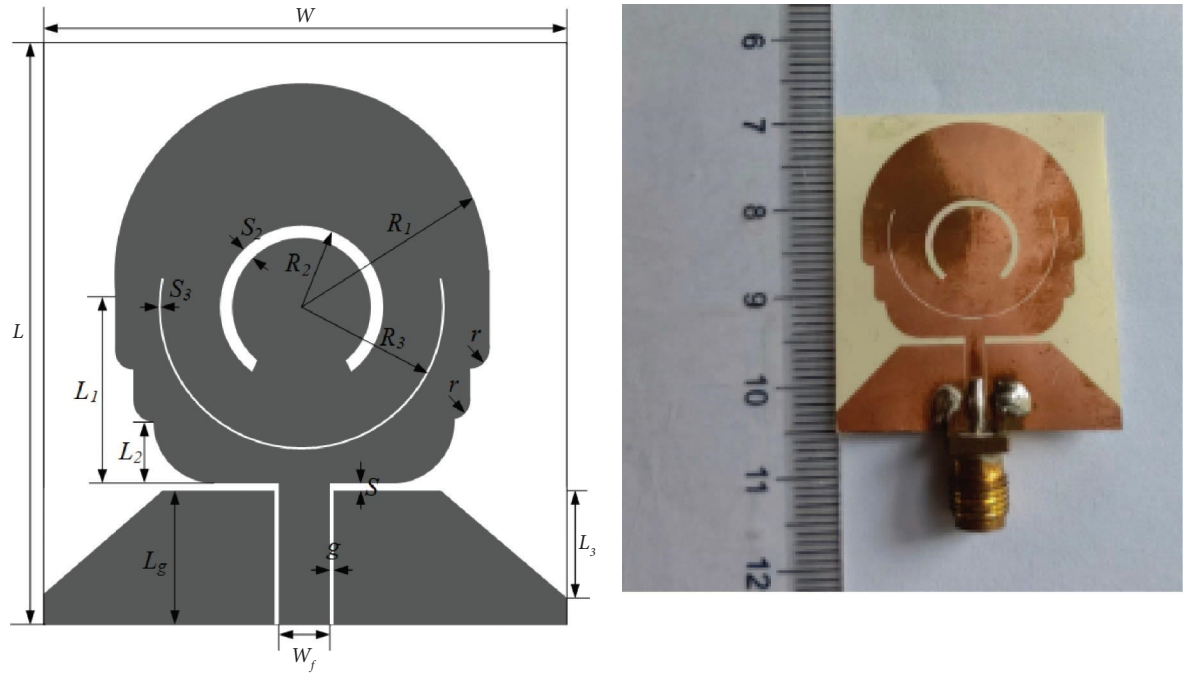

(a) (b)

Figure 1: (a) Antenna structure schematic. (b) Antenna physical diagram.

Table 1: Antenna size parameters (unit: mm).

Parameter	Value
L	35
W	30
W_f	2
L_1	12
L_2	3.9
L_3	7
L_g	9.2
g	0.13
r	1
R_1	12
R_2	4.7
R_3	9
S_2	0.8
S_3	0.2
S	0.8
h	0.1

2.3. Impedance Characteristics Analysis of the Antenna. In the design of the ultra-wideband antenna, the height of the ground plate Lg and the gap between the ground plate and the feed line g are two important parameters to simulate and analyze the impact on the impedance characteristics of the antenna, and the simulation curve is shown in Figure 4. From Figure 4(a), we can see that Lg takes the value of the change, and the antenna performance at high frequency has a certain impact and almost no impact on the low frequency part. As the value of Lg increases, the bandwidth at high frequency gradually decreases, so we take Lg as 9.2 mm. Figure 4(b) shows that, with the gap between the ground plate and the feed line g value becoming smaller, S_{11} parameters in the ultra-broadband band to −10 dB, so take g as 0.13 mm.

2.4. Analysis of the Trap Characteristics of the Antenna. Figure 1(a) depicts the antenna structure. The trap function is introduced by etching slits on the radiating patch. Figure 5 shows the simulation curve. The frequency of the blocking band can be influenced by the width of the slot line and the radius of the two etched C-shaped slits.

The effect on the trapping characteristics is simulated and analyzed by using the radius R_3 of the relatively large C-shaped slit and the width S_2 of the relatively small C-shaped slit. As seen in Figure 5(a), the trap center frequency shifts to the low frequency with an increase in the radius R_3 of the C-shaped slit. The relatively wide C-shaped slit causes the antenna to trap in the WiMAX band, while the comparatively small C-shaped slit causes the antenna to trap in the WLAN band. As the width of the C-shaped slit S_2 grows in Figure 5(b), the WLAN trap band center frequency changes to higher frequencies.

3. Results and Discussion

This section discusses the various performances of the antenna based on Ansoft HFSS 19 and Keysight N5234A PNA-L vector network analyzer.

3.1. S-Parameters. Figure 6(a) displays the results of the simulation for both the proposed antenna and the measured S_{11}. Two blocking bands are generated at 3.20–4.10 GHz and 5.19–5.98 GHz, whereas the antenna's simulated operational bandwidth at 1.96–11.61 GHz. Although there is a slight shift in the operating frequency of the low-frequency part and the trap center frequency due to the measurement environment, physical welding, and RF connection line loss, the measured

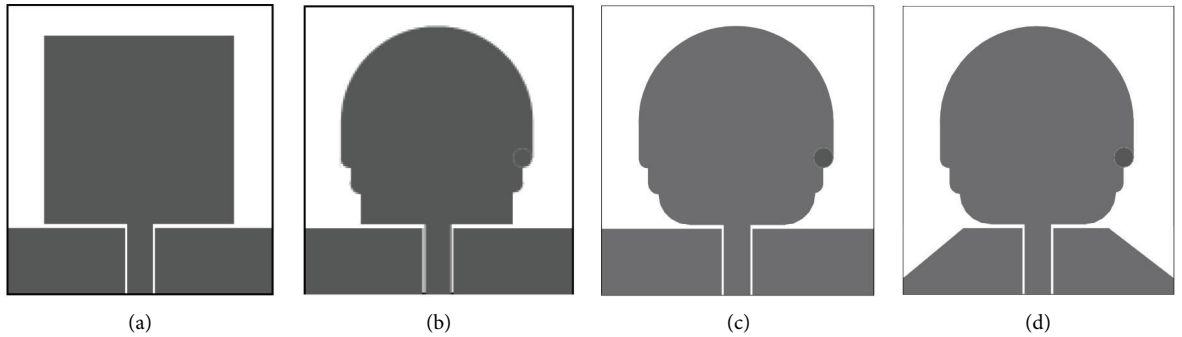

Figure 2: Antenna design flow. (a) Ant-a. (b) Ant-b. (c) Ant-c. (d) Ant-d.

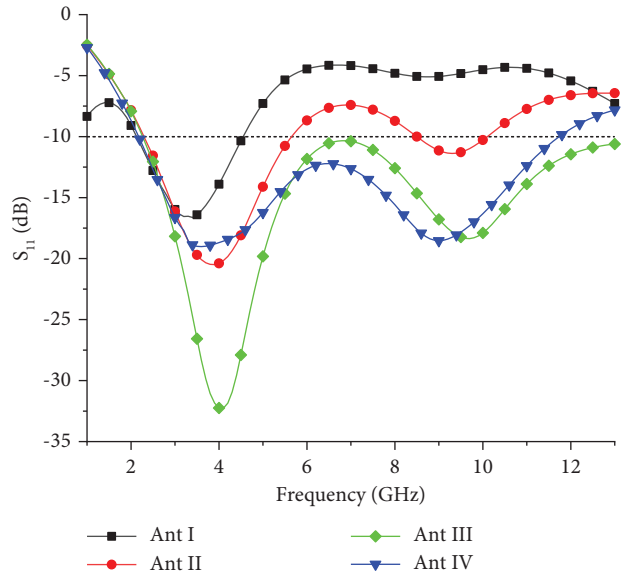

Figure 3: S-parameters of four types of antennas.

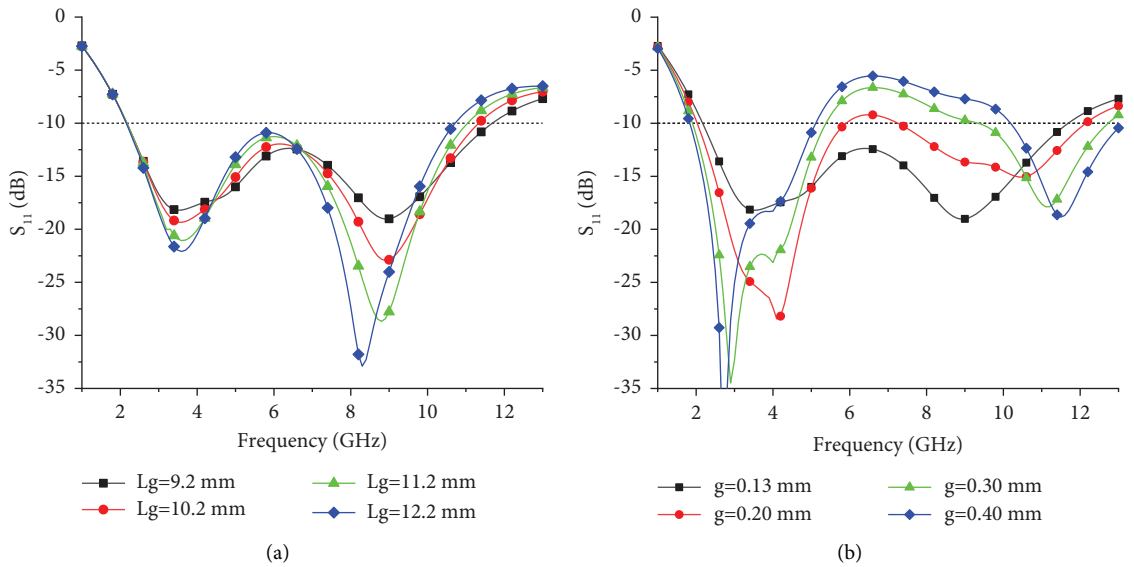

Figure 4: Effect of different Lg and g taking values on S_{11}.

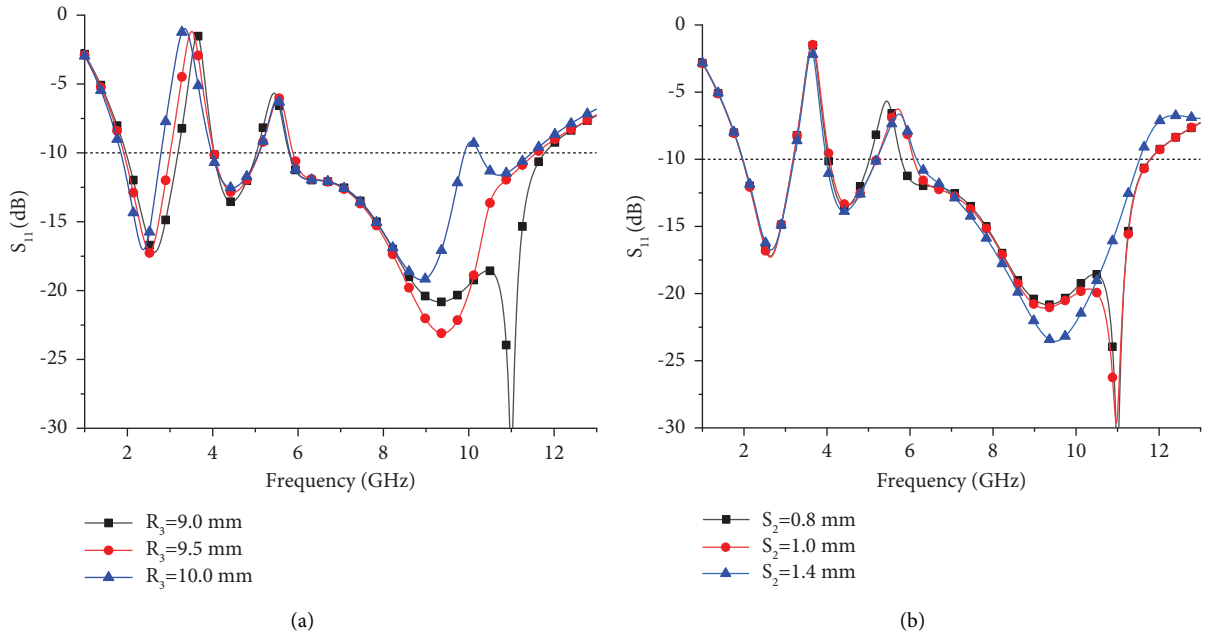

Figure 5: Effect of different values of R_3 and S_2 on S_{11}.

operating bandwidth still satisfies the requirements of the ultra-wide band. Overall, the measured results are essentially consistent with the simulated results.

Figure 6(b) gives the antenna simulation and the measured antenna gain; by the test environment, the measured antenna gain at low frequency is slightly lower than the simulated gain, but at high frequency, it is better than the simulated gain; the gain can reach 7.78 dB, and in the trap band, the gain has a significant reduction, indicating that the antenna cannot work properly in the trap band and can shield the interference of the two trap bands.

3.2. Current Distribution. In order to analyze the trap characteristics of the antenna, two trap frequencies of 3.6 GHz and 5.4 GHz are selected, and the current distribution on the antenna's surface is then simulated and examined, as illustrated in Figure 7. When the antenna operates at 3.6 GHz, the feed line and the relatively large C-shaped slit receive the majority of the antenna surface current. Since the current flowing in both directions from either side of the slit is opposite at this point, the generated fields cancel each other out and are unable to radiate out effectively, which results in the trap characteristics. When the antenna works at 5.4 GHz, the surface current is mainly concentrated at the relatively small C-shaped slit and the feed line.

3.3. Radiation Patterns. Figure 8 shows the anechoic chamber environment at the time of the antenna's actual radiation direction diagram. Figures 9(a)–9(d) show the simulated radiation patterns of the antenna at 3 GHz, 5 GHz, 7 GHz, and 9 GHz, respectively. As can be seen from this figure, the *H* surface of the antenna is approximately circular, the radiation pattern of the antenna is approximately omnidirectional and does not change much within the operating bandwidth, and the *E* surface of the antenna is "8" shaped. Work in the high-frequency band will produce more electromagnetic waves, and the direction of maximum radiation will change. Overall, the radiation properties of the antenna in the working band range are good. The measured direction of the antenna is shown in Figures 10(a)–10(d). The test environment is to blame for the modest distortion of the observed radiation direction map. The omnidirectional antenna's radiation properties are affected by the bracket that was installed behind it during testing, making it impossible to measure the radiation direction map of the antenna correctly in an anechoic chamber.

3.4. Flexible Properties. With a relative permittivity of 2.9 and a loss angle tangent of 0.002, liquid crystal polymer (LCP) material is used as the dielectric substrate in this paper's ultra-wideband antenna design. LCP is a flexible material that exhibits good flexibility, allowing the antenna to be bent and conformal to the carrier surface with good molding performance. In addition, LCP offers a broad research prospect in the field of wearable antennas.

Figure 11(a) depicts the antenna's bending simulation design. The antenna is bent horizontally, and the influence on the antenna's S_{11} characteristics under various bending radii is simulated. R_i represents the bending radius. Then, as indicated in Figure 11(b), R_j is chosen as the bending radius, and the impact of bending in a vertical direction on the antenna's S_{11} characteristics is examined and simulated. The simulated S_{11} parameters for the antenna bending in both the horizontal and vertical directions are shown in Figures 12(a) and 12(b), respectively. When the antenna is bent along the horizontal and vertical directions, the operating bandwidth at high frequency becomes smaller compared

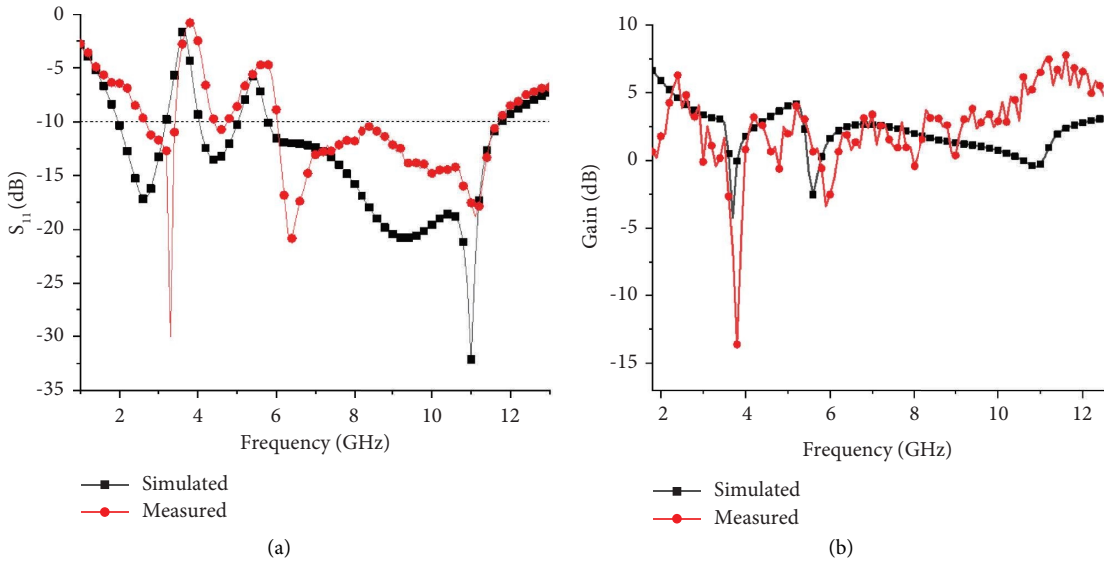

Figure 6: Simulated and measured antenna' S-parameters and gain.

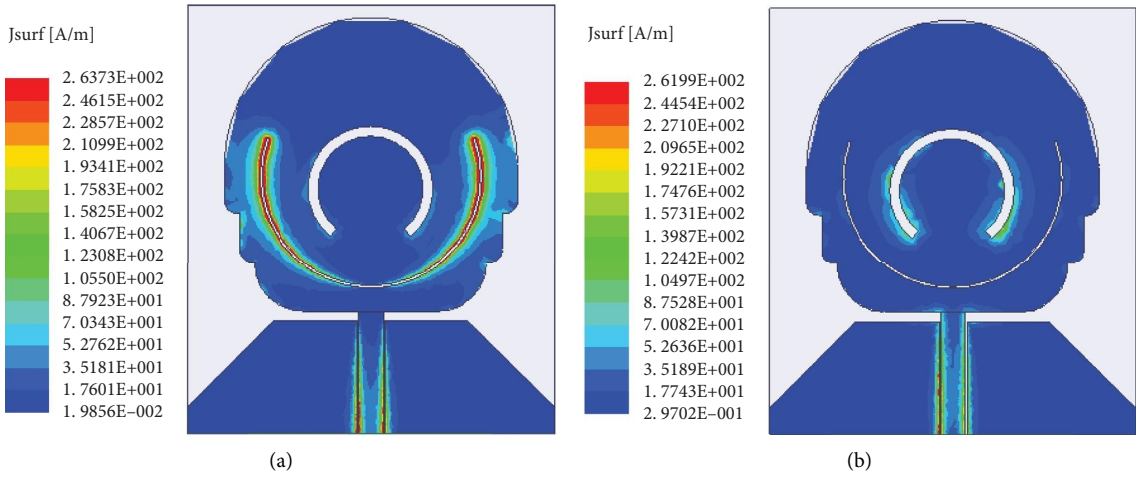

Figure 7: Current distribution at the trap frequency of the antenna. (a) 3.6 GHz. (b) 5.4 GHz.

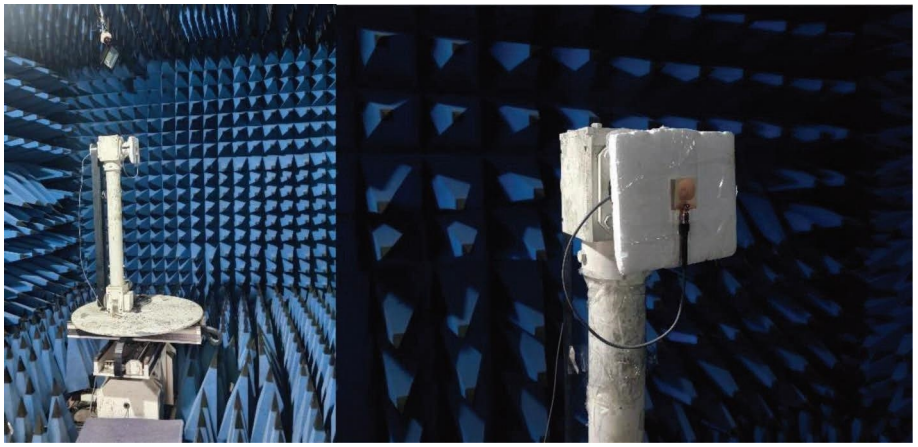

Figure 8: Anechoic chamber measurement environment.

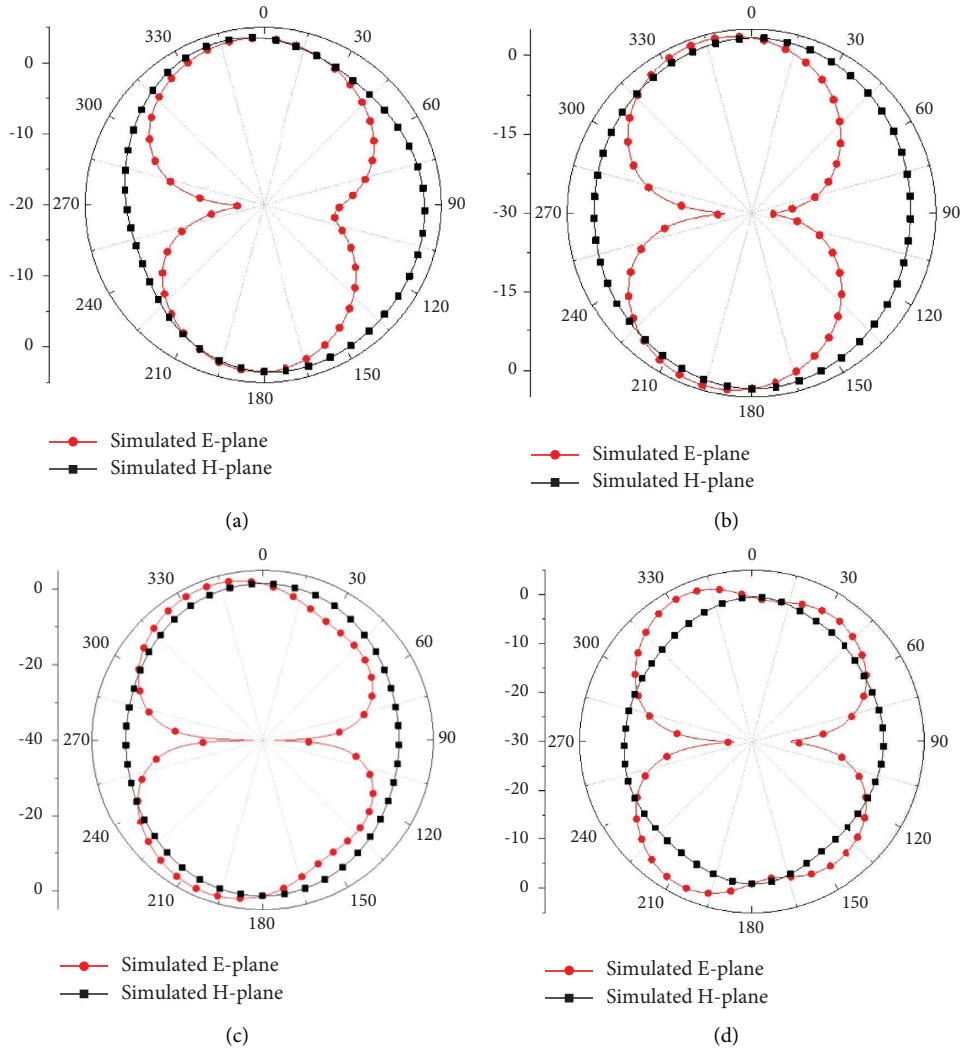

Figure 9: Simulated radiation patterns of the antenna at different frequencies. (a) 3 GHz. (b) 5 GHz. (c) 7 GHz. (d) 9 GHz.

with the simulation results when it is flat, but the effect on the operating bandwidth at low frequency is almost insignificant, which can still meet the demand of ultra-wideband communication systems. The antenna is then coformed with cylinders of varying radii; these radii are the bending radii R_i and R_j. The S_{11} parameters of the antenna under various bending radii are then measured, and the measured results of the antenna bending are displayed in Figures 12(a) and 12(b). The center frequencies of the two trap bands will be somewhat impacted by the increase in the bending radius; the WiMAX band trap center frequency remains almost unchanged, while the WLAN band trap center frequency shifts to a lower frequency in comparison to its flat state. However, the bandwidth of the trap band remains essentially unchanged, and the overall trend can still meet the requirements.

3.5. The Effect of the Human Body on the Antenna. In order to verify the wearability of the antenna, the designed antenna is placed on the human chest position, arms, and legs to measure the return loss S_{11}, so as to verify the impact of the human body on the antenna performance, and the placement position is shown in Figure 13. The antenna is placed on the clothing and the human body conformal will have a slight bend; the measurement results are given, the low-frequency part of the operating band and the center frequency of the trapped wave and the horizontal placement of the measurement results change slightly, but basically can meet the design requirements.

3.6. Human-Specific Absorption Rate Simulation. The human simulation model, as illustrated in Figure 14, is established in accordance with the literature [21] to verify the scenario of the flexible antenna applied to the body domain network. The analysis of the SAR value of the human body-specific absorption rate is used to measure the effect of the radiated energy on the human tissue during the operation of the flexible antenna. The dimensions of the human body model are $45 \times 50 \times 40\ \text{mm}^3$. It is composed of four layers: a skin layer that is 2 mm thick, with a conductivity of $\sigma = 1.49$ (S/m) and

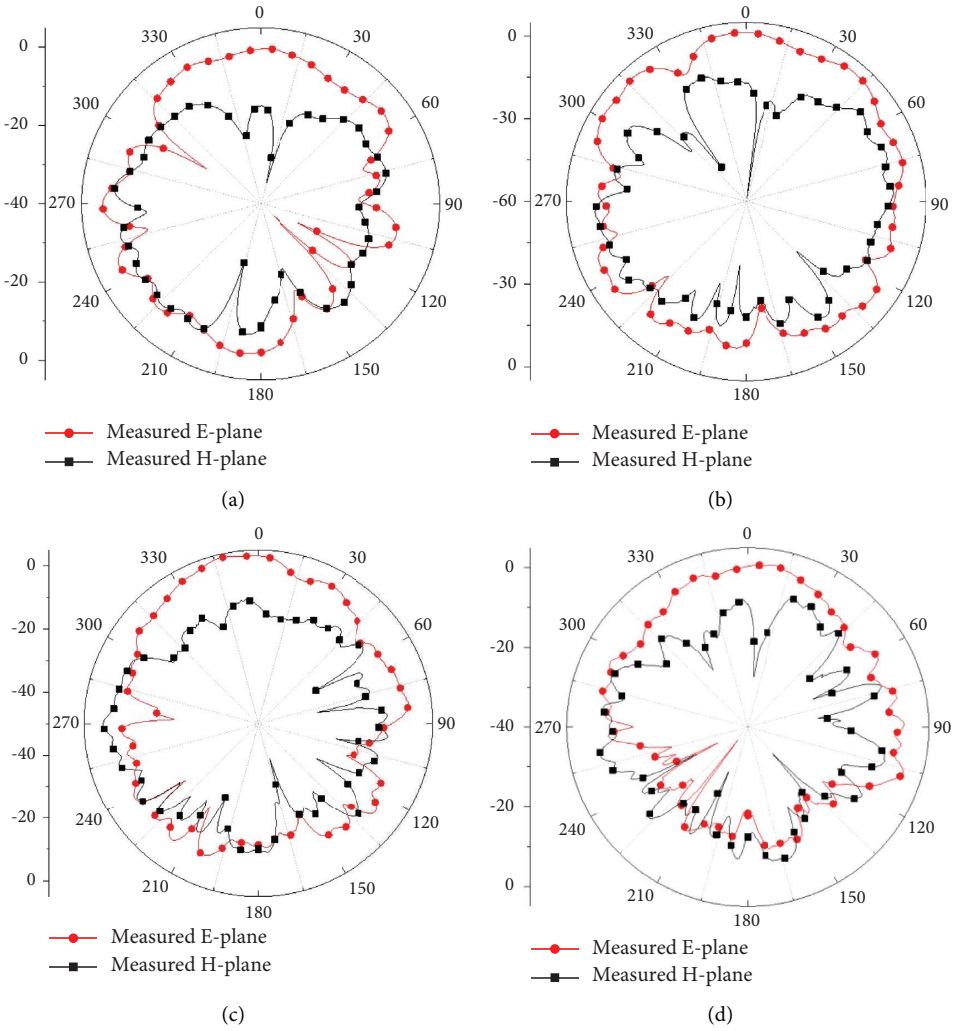

Figure 10: Measured radiation patterns of the antenna at different frequencies. (a) 3 GHz. (b) 5 GHz. (c) 7 GHz. (d) 9 GHz.

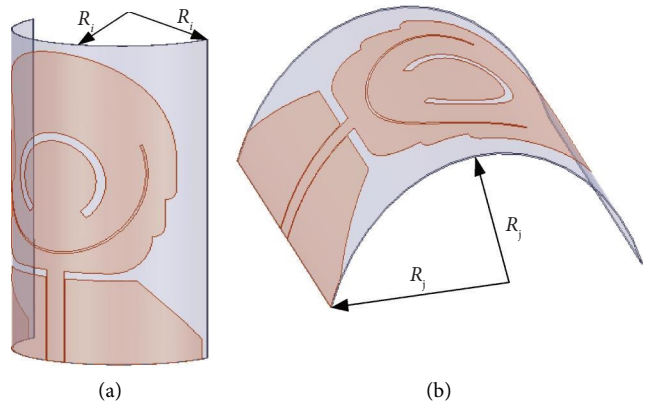

Figure 11: Schematic diagram of the antenna under different directions of bending. (a) Bending along the horizontal direction. (b) Bending along the vertical direction.

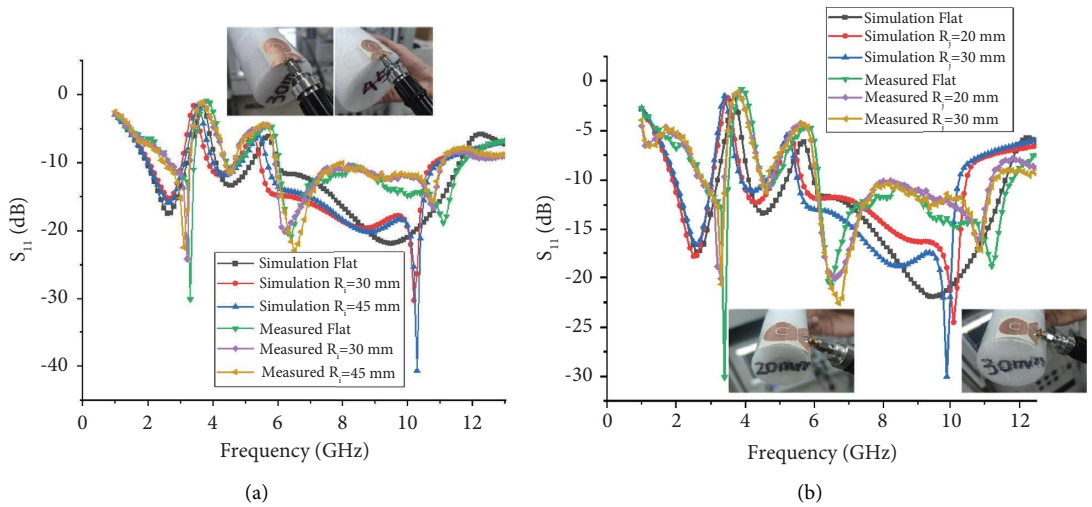

Figure 12: Effect of bending in different directions on S_{11}. (a) Bending along the horizontal direction. (b) Bending along the vertical direction.

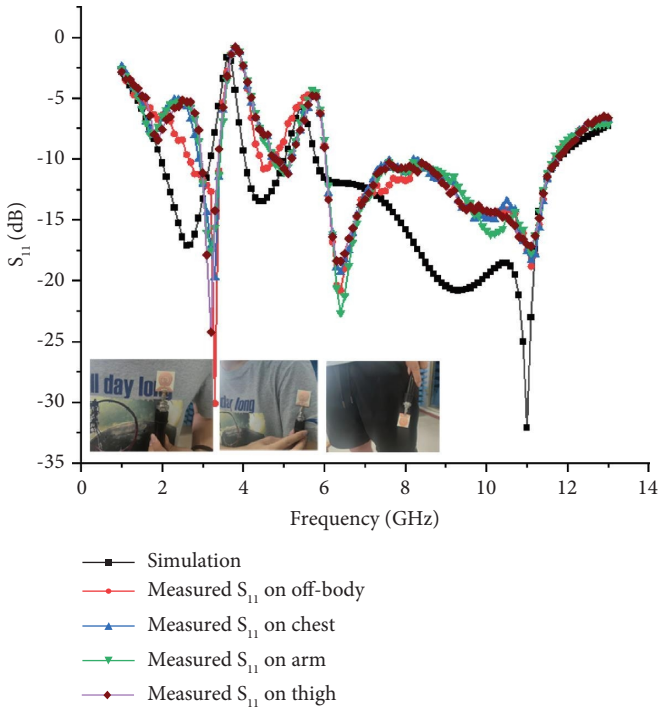

Figure 13: Antenna placed on the human body' S_{11} parameters.

a dielectric constant of $\varepsilon_r = 37.59$; a fat layer that is 5 mm thick, with a dielectric constant of $\varepsilon_r = 5.27$ and a conductivity of $\sigma = 0.11$ (S/m); a 20 mm thick model, representing the muscle model, and a 13 mm thick model, representing the bone model, with a dielectric constant of $\varepsilon_r = 18.49$ and a conductivity of $\sigma = 0.82$ (S/m). The SAR values are calculated as follows:

$$\text{SAR} = \frac{\sigma E^2}{\rho}, \tag{2}$$

where E is the root mean square value of the electric field strength, ρ is the density of human tissue, and σ is the electrical conductivity. Table 2 displays the highest SAR values that were obtained from the simulation at various operating frequencies when the input power was set to 0.2 W and the distance between the antenna and the human tissue model was $h_1 = 5$ mm. The human body simulation model is established for SAR value simulation [22]. The highest SAR value of 10 g of human tissue is less than 2 W/kg, which is lower than the EU standard for all simulated maximum SAR values. Assuming a distance of $h_1 = 5$ mm between the antenna and the human tissue model, Figure 15 displays the SAR distribution on the 10 g model at various operating frequencies. The comprehensive comparison between this work and some other wideband antennae is conducted in Table 3.

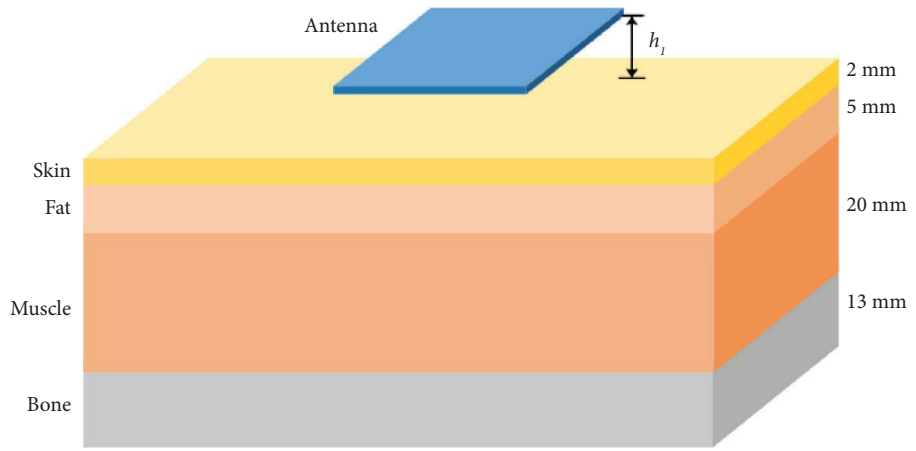

Figure 14: Human tissue model.

Table 2: Maximum SAR values at different frequencies.

Frequency (GHz)	10 g tissue (W/kg)
3.5	1.39
6	1.05
9.5	1.11

Table 3: Comparison of several types of antennas.

References	Size (mm^3)	Trapped wave	Bandwidth (GHz)	Substrate	Feed	Max gain (dB)	Max SAR (W/kg)	Flexibility
[23]	$32.5 \times 20.5 \times 1.6$	0	2.8–12	FR4	Microstrip line	6.5	Not mentioned	No
[24]	$72 \times 72 \times 1.2$	1	3–12	FR4	Microstrip line	6.8	Not mentioned	No
[25]	$22 \times 13 \times 0.8$	1	2.9–23.5	Taconic TLY-5	Microstrip line	Not mentioned	Not mentioned	No
[26]	$22 \times 15 \times 1.6$	0	3.4–12.9	FR4	Microstrip line	Not mentioned	Not mentioned	No
[27]	$30 \times 23 \times 0.5$	0	2.45/5.8	PI	Microstrip line	6.89	0.39	Yes
[28]	$50 \times 40.6 \times 0.075$	0	2.02–2.92	PI	CPW	Not mentioned	Not mentioned	Yes
[29]	$30 \times 30.5 \times 1$	0	4.0–13.6	PDMS	Microstrip line	5.91	1.99	Yes
This article	$30 \times 35 \times 0.1$	2	1.96–11.61	LCP	CPW	7.78	1.39	Yes

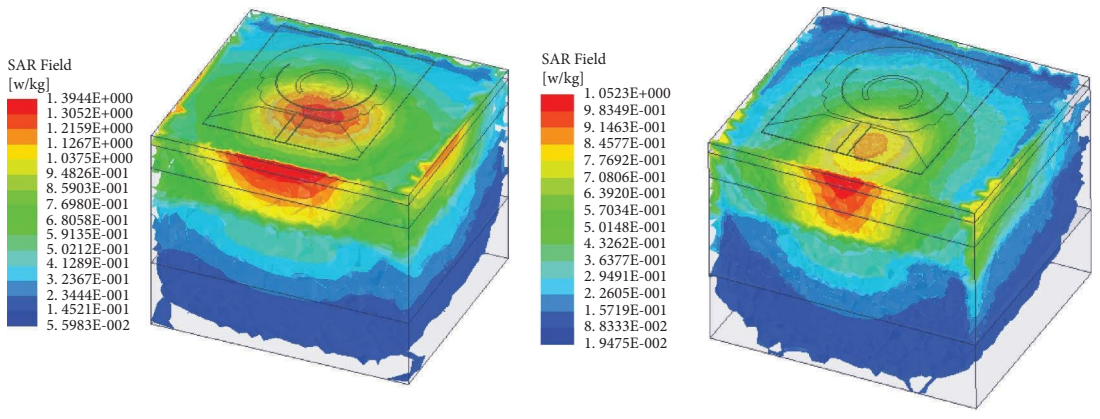

(a) (b)

Figure 15: Continued.

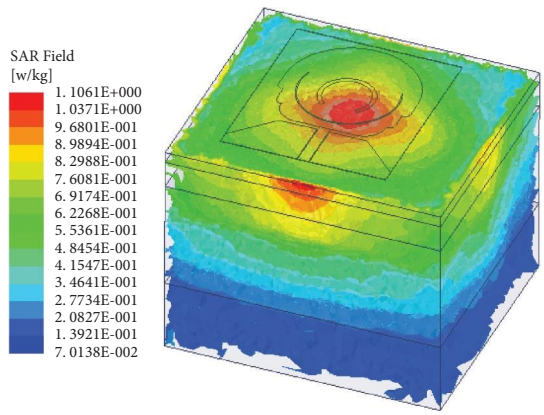

(c)

Figure 15: SAR distribution of 10 g of tissue simulated on the human tissue model at different operating frequencies. (a) 3.5 GHz. (b) 6 GHz. (c) 9.5 GHz.

4. Conclusion

In this paper, a flexible liquid crystal polymer-based trapped ultra-wideband antenna is designed, constructed, and its dimensions, number of traps, operational bandwidth, dielectric substrate type, feeding mechanism, and bending properties are compared with those of contemporary literature. By using liquid crystal polymer flexible material as the dielectric substrate, the coplanar waveguide for feeding, and etched C-shaped slits on the radiating patch to fulfill the trap function; this research designs a wearable ultra-wideband flexible antenna for usage in body domain networks. Experiments were conducted on the effects of flexible bending and human-specific absorption rate of the antenna. The antenna operates in the frequency band range of 1.96–11.61 GHz and suppresses interference in the WiMAX band and WLAN band. The results demonstrate the good radiation characteristics, good gain, good bending characteristics in the working band, and good radiation performance to the human body of the antenna designed in this paper. It can be used for applications in the body area network and ultra-wideband communication systems.

Data Availability

The data used to support the findings of this study are included within the article.

Conflicts of Interest

The authors declare that they have no conflicts of interest regarding the publication of this paper.

Acknowledgments

This work was supported by the Shaanxi Provincial Department of Science and Technology Key R&D Fields Industrial Tackling Project (2022GY-094).

References

[1] S. X. Ta and I. Park, "Multiband-notched UWB antenna using folded slots in the feeding structure," *Journal of electromagnetic engineering and science*, vol. 14, no. 1, pp. 31–35, 2014.

[2] P. B. Samal, P. J. Soh, and G. A. E. Vandenbosch, "UWB all-textile antenna with full ground plane for off-body WBAN communications," *IEEE Transactions on Antennas and Propagation*, vol. 62, no. 1, pp. 102–108, 2014.

[3] O. P. Kumar, P. Kumar, and T. Ali, "A compact dual-band notched UWB antenna for wireless applications," *Micromachines*, vol. 13, no. 1, p. 12, 2021.

[4] S. Park and K. Y. Jung, "Novel compact UWB planar monopole antenna using a ribbon-shaped slot," *IEEE Access*, vol. 10, pp. 61951–61959, 2022.

[5] M. C. Tang, Z. Chen, and R. W. Ziolkowski, "Compact printed ultra-wideband antenna: corrugated monopole augmented with parasitic strips," *Journal of Electromagnetic Waves and Applications*, vol. 30, no. 13, pp. 1702–1711, 2016.

[6] M. Bahare, B. V. B. S. Roy, H. R. Maqsood, C. O. Yann, Z. Maxim, and S. Ronan, "A conformal band-notched ultrawideband antenna with monopole-like radiation characteristics," *IEEE Antennas and Wireless Propagation Letters*, vol. 19, no. 1, pp. 203–207, 2019.

[7] M. Gupta and V. Mathur, "A new printed fractal right angled isosceles triangular monopole antenna for ultra-wideband applications," *Egyptian Informatics Journal*, vol. 18, no. 1, pp. 39–43, 2017.

[8] S. W. Kim and D. Y. Choi, "Implementation of rectangular slit-inserted ultra-wideband tapered slot antenna," *Springer Plus*, vol. 5, no. 1, pp. 1387–1398, 2016.

[9] R. Neda, A. Mohammad, and S. Abdelrazik, "Controllable triple band-notched monopole antenna for ultra-wideband applications," *IET Microwaves, Antennas and Propagation*, vol. 9, no. 4, pp. 336–342, 2015.

[10] A. S. Abd El-Hameed, M. G. Wahab, N. A. Elshafey, and M. S. Elpeltagy, "Quad-Port UWB MIMO antenna based on LPF with vast rejection band," *AEU-International Journal of Electronics and Communications*, vol. 134, Article ID 153712, 2021.

[11] P. Kumar, S. Urooj, and F. Alrowais, "Design and implementation of quad-port MIMO antenna with dual-band elimination characteristics for ultra-wideband applications," *Applied Sciences*, vol. 10, no. 5, p. 1715, 2020.

[12] P. Pannu and D. K. Sharma, "A low-profile quad-port UWB MIMO antenna using defected ground structure with dual notch-band behavior," *International Journal of RF and Microwave Computer-Aided Engineering*, vol. 30, no. 9, Article ID 22288, 2020.

[13] Z. Li, C. Yin, and X. Zhu, "Compact UWB MIMO Vivaldi antenna with dual band-notched characteristics," *IEEE Access*, vol. 7, pp. 38696–38701, 2019.

[14] S. Raziul Ahasan, K. Islam, M. Monirujjaman Khan, M. Masud, G. Singh Gaba, and H. A Alhumyani, "Novel compact UWB band notch antenna design for body-centric communications," *Computer Systems Science and Engineering*, vol. 40, no. 2, pp. 673–689, 2022.

[15] Z. Chen, W. Zhou, and J. Hong, "A miniaturized MIMO antenna with triple band-notched characteristics for UWB applications," *IEEE Access*, vol. 9, pp. 63646–63655, 2021.

[16] L. S. Yang, M. Xu, and C. Li, "Four-element MIMO antenna system for UWB applications," *Radio Engineering*, vol. 27, no. 1, pp. 60–67, 2019.

[17] A. Chandra and R. Kumar, "Development of wideband CPW-fed hexagon-shaped circularly polarized slot antenna for wireless-communications," *International Journal of Communication Systems*, vol. 36, Article ID e5503, 2023.

[18] W. T. Li, Y. Q. Hei, P. M. Grubb, X. W. Shi, and R. T. Chen, "Compact inkjet-printed flexible MIMO antenna for UWB applications," *IEEE Access*, vol. 6, pp. 50290–50298, 2018.

[19] H. Yalduz, T. E. Tabaru, V. T. Kilic, and M. Turkmen, "Design and analysis of low profile and low SAR full-textile UWB wearable antenna with metamaterial for WBAN applications," *AEU-International Journal of Electronics and Communications*, vol. 126, Article ID 153465, 2020.

[20] T. Annalakshmi and S. Ramesh, "Performance and analysis of UWB aesthetic pattern textile antenna for WBAN applications," *Applied Computational Electromagnetics Society*, vol. 35, no. 12, pp. 1525–1531, 2021.

[21] C. Du and G. Jin, "A compact CPW-fed band-notched UWB-MIMO flexible antenna for WBAN application," *Journal of Electromagnetic Waves and Applications*, vol. 35, no. 8, pp. 1046–1058, 2021.

[22] A. Verma, R. K. Arya, R. Bhattacharya, and S. N. Raghava, "Compact PIFA antenna with high gain and low SAR using AMC for WLAN/C-band/5G applications," *IETE Journal of Research*, vol. 69, no. 7, pp. 4422–4432, 2023.

[23] K. H. Alharbi, M. Moniruzzaman, R. W. Aldhaheri et al., "Ultra-wideband monopole antenna with U and L shaped slotted patch for applications in 5G and short distance wireless communications," *International Journal of Applied Electromagnetics and Mechanics*, vol. 66, no. 1, pp. 159–180, 2021.

[24] M. Wang, H. Wang, P. Chen, T. Y. Ding, J. Xiao, and L. Zhang, "A butterfly-like slot UWB antenna with WLAN band-notch characteristics for MIMO applications," *IEICE Electronics Express*, vol. 19, no. 14, Article ID 20220233, 2022.

[25] N. Hussain, M. Jeong, J. Park, S. Rhee, P. Kim, and N. Kim, "A compact size 2.9-23.5 GHz microstrip patch antenna with WLAN band-rejection," *Microwave and Optical Technology Letters*, vol. 61, no. 5, pp. 1307–1313, 2019.

[26] J. C. Nan, M. H. Wang, M. M. Gao, and J. Liu, "Miniaturized inverted ultra-wideband multiple-input multiple-output antenna with high isolation," *Electronics Letters*, vol. 57, no. 3, pp. 100–102, 2021.

[27] S. Wang and H. Gao, "A dual-band wearable conformal antenna based on artificial magnetic conductor," *International Journal of Antennas and Propagation*, vol. 2022, Article ID 9970477, 8 pages, 2022.

[28] Y. Liu, Z. L. Wang, D. Y. Cang, J. S. Gong, and H. W. Qu, "A polyimide-based flexible monopole antenna," *Journal of Materials Science: Materials in Electronics*, vol. 33, no. 3, pp. 1686–1702, 2022.

[29] M. A. Nirmal, S. P. Kumar, Y. V. Prakash, P. P. Omprakash, and Solanki, "Design and analysis of an edge truncated flexible antenna for wi-fi applications," in *Proceedings of the 2022 International Conference on Electronics and Renewable Systems (ICEARS 2022)*, pp. 1861–1864, Tuticorin, India, March, 2022.